**(Preprint) AAS 24-168**

# ANGLES-ONLY ROBUST TRAJECTORY OPTIMIZATION FOR NRHO RENDEZVOUS

**Timothy Cavesmith[*], David Woffinden[†], Nathan Collins[‡]**

This study demonstrates a robust trajectory optimization approach for rendezvous and proximity operations with angles-only navigation measurements. Often, sensors that directly measure relative range and velocity require communication or coordination between the chaser and target vehicle and can have limiting pointing accuracy, mass, or power requirements compared to angle measurement sensors. Thus, the capability to perform a rendezvous with only angle measurements can be advantageous for vehicle design and to improve robustness to failures. However, the well studied limitation of angles-only navigation in measuring range results in large uncertainties in the navigation system that must be reduced with known chaser vehicle translational maneuvers to induce observability in range for the navigation filter. This analysis presents a trajectory optimization problem for a lunar ascent rendezvous during a crewed lunar mission in a Near-Rectilinear Halo Orbit (NRHO) that is limited to only angle measurements. The objective of this study is to show that an angles-only rendezvous is feasible in an NRHO and to present the sensitivity to an assortment of constraints generated from a systematic optimization process using linear covariance analysis and particle swarm optimization. Linearized NRHO dynamics and linearized relative targeting are applied to use linear covariance analysis to determine the expected $\Delta$v and trajectory dispersions due to initial state uncertainty, sensor errors, maneuver execution errors, and unmodeled dynamics. The $\Delta$v and trajectory dispersions are passed into a particle swarm optimization algorithm to find the optimized maneuver profile that minimizes propellant use while satisfying constraints such as free drift and underburn to $3\sigma$ certainty. The trajectory constraints including time available, desired final uncertainty, and initial uncertainty are varied to ascertain sensitivity and desirable engineering trades.

## INTRODUCTION

As interest in exploring the lunar poles grows, space programs around the world are planning and executing missions to cislunar space with unprecedented complexity and scale. NASA's Artemis program plans to land human explorers on the moon and focuses its operations in an Earth-Moon L2 Near Rectilinear Halo Orbit (NRHO) due to its favorable communication and thermal properties and its transfer options to Earth, other cislunar orbits, the lunar surface, and beyond.[1] With the need to perform rendezvous and proximity operations in this new flight regime shown in Figure 1, which has yet to be flown by humans, robust plans will be critical for mission success and crew safety. When selecting sensor suites and designing trajectories in this new environment, mission planners must account for uncertainties in the guidance, navigation, and control system (GN&C). Ideally, the selection of reference trajectories, navigation requirements, and mission constraints would account for expected and worst-case integrated GN&C performance in the presence of initial state uncertainties, measurement errors, maneuver execution errors, and uncertainties in the environmental dynamics model.[2] In this text, *robust* trajectory design refers to techniques that account for such uncertainties in GN&C performance. A trajectory *optimization* refers to using techniques to minimize a parameter such as propellant use. Thus, the *robust trajectory optimization* process in this study generates maneuver profiles that use minimal propellant while meeting specified mission objectives and constraints to a high probability (corresponding to $3\sigma$ from the expected value in this analysis).

[*]Cadet, Department of Astronautics, United States Air Force Academy, USAF Academy, CO, 80840
[†]Aerospace Engineer, GN&C Autonomous Flight Systems Branch, NASA Johnson Space Center, Houston TX, 77058
[‡]Assistant Professor of Astronautics, Department of Astronautics, United States Air Force Academy, USAF Academy, CO, 80840

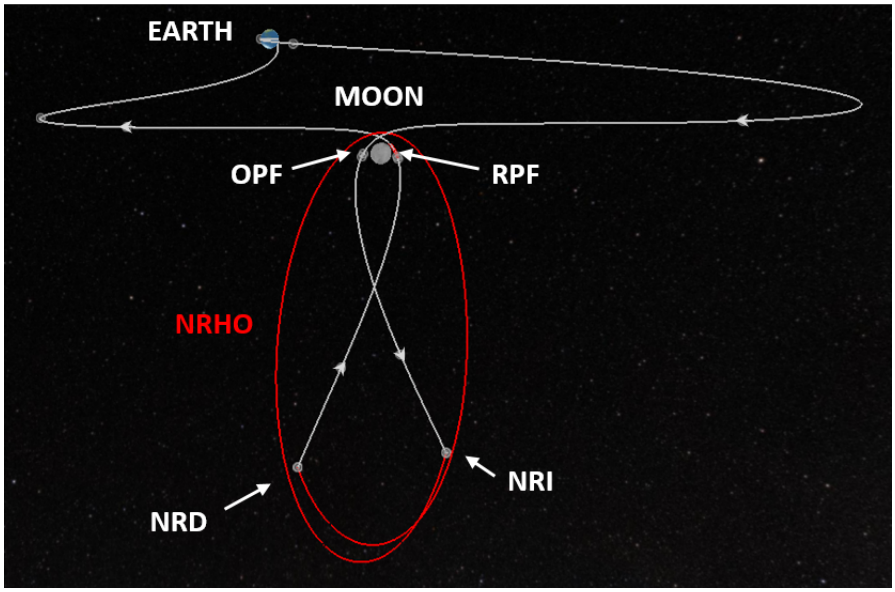


**Figure 1**: Notional cislunar trajectory to NRHO

The conventional method of characterizing GN&C system performance in the presence of uncertainties involves using Monte Carlo analysis to find the distribution of $\Delta$v and trajectory dispersions for a given reference (nominal) trajectory.[3] This is computationally intensive with lengthy run times because Monte Carlo simulations involve running the specific reference trajectory hundreds or thousands of times with random variables to generate statistical information ($3\sigma$ dispersions). Thus, a Monte Carlo simulation to evaluate a single reference trajectory might take on the order of minutes or hours. While this is feasible for validation, such a technique would be infeasible for use in a numerical optimization process, which might require evaluating hundreds or thousands of reference trajectory candidates to find the global minimum solution. Since the rendezvous scenario presented in this work includes safety constraints that are enforced with penalties, the cost function becomes non-continuous and thus non-differentiable. This prevents the use of faster optimization algorithms such as gradient descent. This work utilizes particle swarm optimization (PSO) to minimize the trajectory cost function due to its ease of implementation and accuracy at finding the global optimal solution, but previous robust optimization processes have utilized a genetic algorithm.[4]

Using Monte Carlo analysis to evaluate the hundreds or thousands of reference trajectories in the optimization loop would take days or weeks. Instead, this work uses linear covariance analysis (LinCov) to determine the equivalent statistical GN&C performance because it is significantly faster. LinCov determines these metrics by directly propagating (dynamics), updating (measurements), and correcting (impulsive translational maneuvers) the covariance of the state dispersions and navigation error in time with a single simulation run. This is possible by linearizing the dispersion dynamics, the navigation update equation, and the state impulsive correction about the nominal (reference) trajectory at each time step.[5] The nominal trajectory is still propagated with non-linear dynamics. LinCov for robust trajectory optimization has been used for cislunar midcourse correction,[4] rendezvous with range and range-rate measurements,[6] powered descent and landing,[7] and Mars aerocapture[8] and the optimal solution can be validated by Monte Carlo analysis once found.[9] This study expands this robust trajectory optimization technique to angles-only rendezvous trajectories.

As outlined by Raja Chari, angles-only navigation is desirable because simple sensors, including optical and infrared cameras, radio direction finders, and two-way radio systems, can determine the line-of-sight direction.[10] These systems use less power and mass (especially at longer ranges) and can have less stringent pointing accuracy requirements than radar and lidar systems. Additionally, angles-only navigation often has looser cooperation requirements between the chaser and target vehicle than relative GPS and lidar systems. Also, some angles-only techniques provide the potential for passive sensing for stealth, and angles-only

backup plans can provide robustness to systems that already possess a means of acquiring angle measurements. Despite these benefits, a later section in this analysis and previous work[10] show that angles-only navigation has a limitation in determining range. Often, the relative position and velocity cannot be determined with angle measurements alone due to a lack of observability. However, Woffinden shows that observability of a linear system can be guaranteed with a calibrated translational maneuver that generates an alternate line-of-sight profile.[11] The observability burns are most effective when they maximize the change in the line-of-sight profile (or increase the corresponding observability angle). Since adding observability maneuvers to the nominal trajectory adds time and $\Delta$v to the baseline maneuver profile, it is desirable to optimally place these observability burns to minimize total $\Delta$v, which is the sum of nominal propellant usage and $3\sigma$ $\Delta$v dispersions. The optimized profile must robustly adhere to desired performance requirements and safety constraints given uncertainties in integrated GN&C performance. This study analyzes a contingency scenario shown in Figure 2 where astronauts departing the lunar surface in an ascent vehicle must complete a rendezvous to a target vehicle in an NRHO with only angle measurements.

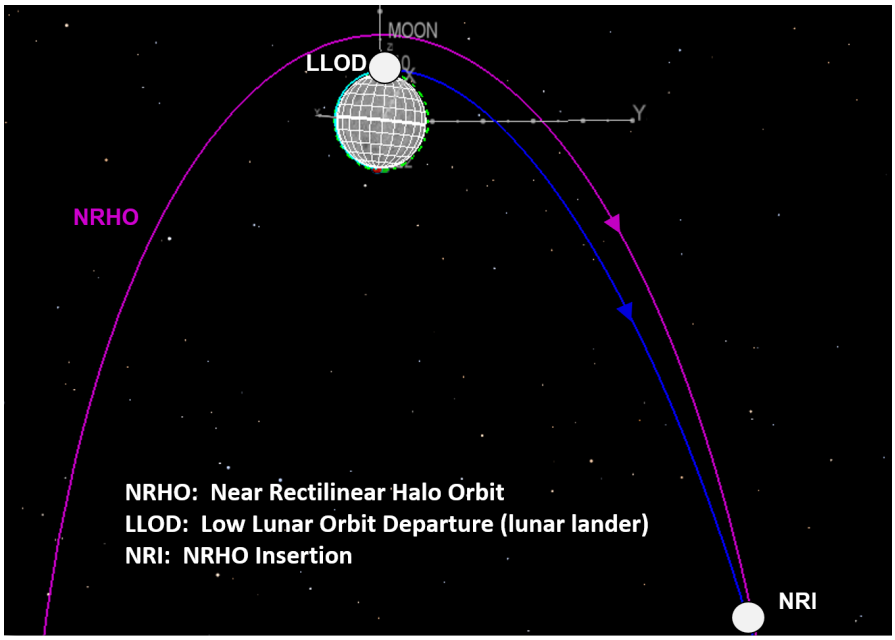


**Figure 2**: Notional departure from lunar surface to NRHO insertion

This paper begins by describing LinCov analysis, trajectory constraints, cost functions, and the optimization method. It also summarizes the linearized NRHO dynamics, impulsive maneuver targeting, and sensor models used in LinCov to propagate, update, and correct a GN&C system's covariance matrix. Then, it compares the statistical GN&C performance of the baseline rendezvous trajectory with direct ranging sensors and angles-only sensor suites. Finally, it presents the results of a trade space analysis, showing how variation in the number of observability burns, the time available to generate observability, allowed final position dispersions from the nominal trajectory (measure of accuracy), and initial state uncertainty (function of ground tracking performance) affects total $\Delta$v in the optimized maneuver profiles.

## ANALYSIS APPROACH

### Performance Metrics

To determine the optimal performance for utilizing an angles-only navigation strategy for NRHO rendezvous, several key performance metrics must be defined to objectively quantify what is acceptable and what constitutes an integrated system failure. These metrics are derived from four states illustrated in Figure

3. The first is the true state $\mathbf{x}$ which is an $n$-dimensional vector that represents the *real world* environment or actual state. The nominal state $\bar{\mathbf{x}}$ is another $n$-dimensional vector that represents the desired or reference state. The navigation state $\hat{\mathbf{x}}$ is an $\hat{n}$-dimensional vector ($\hat{n} < n$) that represents the filter's estimated state. The design state x, often assumed to be the true state, is used to design the onboard navigation filter.

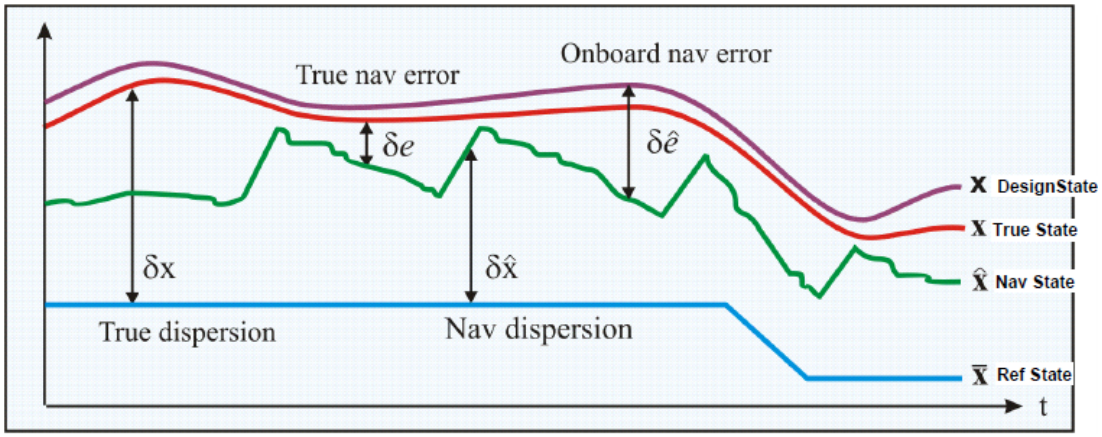


**Figure 3**: GN&C performance metric variables

The variation between these states constitute the actual performance metrics considered in this analysis, also depicted in Figure 3. These include the true trajectory dispersions $\delta\mathbf{x}$, the navigation dispersions $\delta\hat{\mathbf{x}}$, the true navigation error $\delta\mathbf{e}$, and the onboard navigation error $\delta\hat{\mathbf{e}}$. The true dispersions $\delta\mathbf{x}$ are defined as the difference between the true state $\mathbf{x}$ and the nominal state $\bar{\mathbf{x}}$. The covariance matrix of the true dispersions, $\mathbf{D}$, indicates how precisely a GN&C system can follow a desired trajectory.

$$\delta\mathbf{x} \triangleq \mathbf{x} - \bar{\mathbf{x}} \qquad\qquad \mathbf{D} = E\left[\delta\mathbf{x}\delta\mathbf{x}^{\mathrm{T}}\right] \tag{1}$$

The navigation dispersions $\delta\hat{\mathbf{x}}$ are defined as the difference between the navigation state $\hat{\mathbf{x}}$ and the nominal state $\bar{\mathbf{x}}$. The covariance of the navigation dispersions, $\hat{\mathbf{D}}$, reflects how precisely the onboard system thinks it can follow a prescribed reference trajectory.

$$\delta\hat{\mathbf{x}} \triangleq \hat{\mathbf{x}} - \mathbf{M}_x\bar{\mathbf{x}} \qquad\qquad \hat{\mathbf{D}} = E\left[\delta\hat{\mathbf{x}}\delta\hat{\mathbf{x}}^{\mathrm{T}}\right] \tag{2}$$

The matrix $\mathbf{M}_x$ is an $(\hat{n} \times n)$ matrix that maps the estimated state in terms of the true and nominal state. This matrix is necessary to account for the differences in vector length for $\hat{\mathbf{x}}$ and $\bar{\mathbf{x}}$.

The true navigation error $\delta\mathbf{e}$ is the difference between the true state and navigation state. It can also be calculated using the difference between the true dispersions and navigation dispersions. The covariance of the true navigation error, $\mathbf{P}$, quantifies how precisely the onboard navigation system can estimate the true state.

$$\delta\mathbf{e} \triangleq \mathbf{M}_x\mathbf{x} - \hat{\mathbf{x}} = \mathbf{M}_x\delta\mathbf{x} - \delta\hat{\mathbf{x}} \qquad\qquad \mathbf{P} = E\left[\delta\mathbf{e}\delta\mathbf{e}^{\mathrm{T}}\right] \tag{3}$$

The onboard navigation error $\delta\hat{\mathbf{e}}$ itself is never computed, but it is used to develop the onboard navigation filter equations. It is defined as the difference between the design state, x, and the navigation state $\hat{\mathbf{x}}$. The covariance of the onboard navigation error, $\hat{\mathbf{P}}$, quantifies how precisely the onboard navigation system expects it can determine the actual state. The performance of the onboard navigation system is determined by comparing $\hat{\mathbf{P}}$ to the actual navigation performance $\mathbf{P}$.

$$\delta\hat{\mathbf{e}} \triangleq \mathrm{x} - \hat{\mathbf{x}} \qquad\qquad \hat{\mathbf{P}} = E\left[\delta\hat{\mathbf{e}}\delta\hat{\mathbf{e}}^{\mathrm{T}}\right] \tag{4}$$

If the *true* states and the *design* states are assumed to be the same, then the true navigation covariance will equal the onboard navigation covariance.

The covariance matrices of the true dispersions, navigation dispersions, true navigation error, and the onboard navigation error are ultimately used to analyze and assess the performance of a proposed GN&C system. A common approach to obtain these performance metrics is to use a Monte Carlo simulation outlined in Figure 4, where the sample statistics of hundreds or thousands of runs, $N$, are used to numerically compute the desired covariance matrices.

$$\mathbf{D} = \frac{1}{N-1}\sum \delta\mathbf{x}\delta\mathbf{x}^{\mathrm{T}} \qquad \hat{\mathbf{D}} = \frac{1}{N-1}\sum \delta\hat{\mathbf{x}}\delta\hat{\mathbf{x}}^{\mathrm{T}} \qquad \mathbf{P} = \frac{1}{N-1}\sum \delta\mathbf{e}\delta\mathbf{e}^{\mathrm{T}} \tag{5}$$

The onboard navigation error covariance $\hat{\mathbf{P}}$ is the navigation filter covariance for each run.

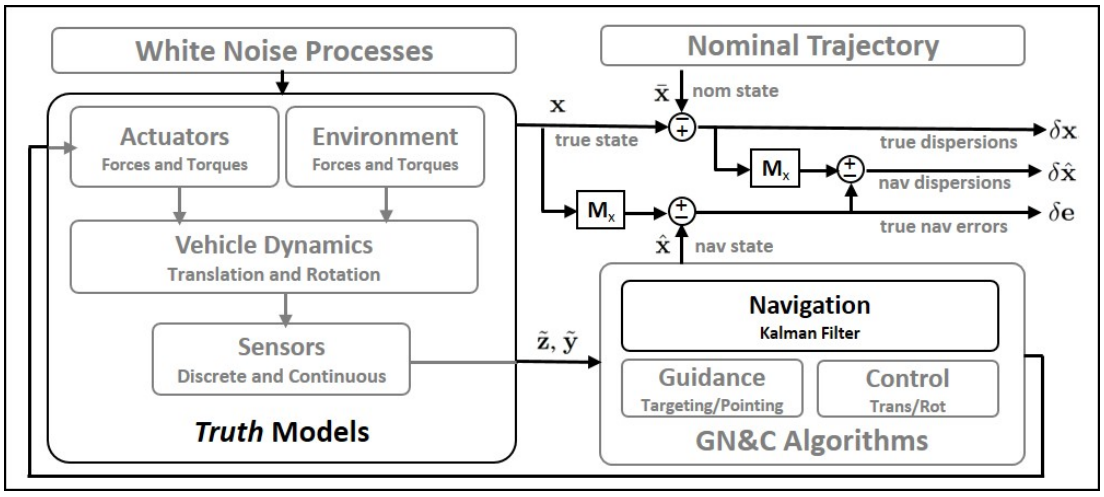


**Figure 4**: Extracting GN&C performance metrics using Monte Carlo techniques

This same statistical information can be obtained using linear covariance analysis techniques. Linear covariance analysis incorporates the non-linear system dynamics models and GN&C algorithms to generate a nominal reference trajectory $\bar{\mathbf{x}}$ which is then used to propagate, update, and correct an onboard navigation covariance matrix $\hat{\mathbf{P}}$ and an augmented state covariance matrix $\mathbf{C}$,

$$\mathbf{C} = E\left[\delta\mathbf{X}\delta\mathbf{X}^{\mathrm{T}}\right] \tag{6}$$

where the augmented state $\delta\mathbf{X}^{\mathrm{T}} = [\delta\mathbf{x}^{\mathrm{T}}\ \delta\hat{\mathbf{x}}^{\mathrm{T}}]$ consists of the true dispersions and the navigation dispersions. Pre- and post-multiplying the augmented state covariance matrix by the following mapping matrices, the covariance matrices of the trajectory dispersions, navigation dispersions, and the navigation error can be obtained with a single simulation run.

$$\begin{aligned}
\mathbf{D} &= [\,\mathbf{I}_{n\times n},\ \mathbf{0}_{n\times\hat{n}}\,]\,\mathbf{C}\,[\,\mathbf{I}_{n\times n},\ \mathbf{0}_{n\times\hat{n}}\,]^{\mathrm{T}} \\
\hat{\mathbf{D}} &= [\,\mathbf{0}_{\hat{n}\times n},\ \mathbf{I}_{\hat{n}\times\hat{n}}\,]\,\mathbf{C}\,[\,\mathbf{0}_{\hat{n}\times n},\ \mathbf{I}_{\hat{n}\times\hat{n}}\,]^{\mathrm{T}} \\
\mathbf{P} &= [\,\mathbf{I}_{\hat{n}\times n},\ -\mathbf{I}_{\hat{n}\times\hat{n}}\,]\,\mathbf{C}\,[\,\mathbf{I}_{\hat{n}\times n},\ -\mathbf{I}_{\hat{n}\times\hat{n}}\,]^{\mathrm{T}}
\end{aligned} \tag{7}$$

**Linear Covariance Analysis**

The linear covariance (LinCov) analysis equations used to propagate, update, and correct both the augmented state covariance matrix and the onboard navigation covariance matrix are summarized here. For additional details regarding the development and implementation of the linear covariance simulation, see the following references.[5,9,12–15]

*LinCov Analysis Modeling* The discrete-time propagation equations for augmented state covariance matrix $\mathbf{C}$ and the onboard navigation covariance matrix $\hat{\mathbf{P}}$ are summarized as previously outlined by Goulet,[6]

$$\mathbf{C}(t_{k+1}) = \mathbf{\Phi}(t_{k+1}, t_k)\mathbf{C}(t_k)\mathbf{\Phi}^T(t_{k+1}, t_k) + \mathbf{G}\mathbf{Q}\mathbf{G}^T \tag{8}$$

$$\hat{\mathbf{P}}(t_{k+1}) = \hat{\mathbf{\Phi}}(t_{k+1}, t_k)\hat{\mathbf{P}}(t_k)\hat{\mathbf{\Phi}}^T(t_{k+1}, t_k) + \hat{\mathbf{G}}\hat{\mathbf{Q}}\hat{\mathbf{G}}^T \tag{9}$$

where $\mathbf{\Phi}$ and $\hat{\mathbf{\Phi}}$ are augmented and onboard state transition matrices, respectively for the linearized perturbation dynamics about the reference trajectory. The mapping matrices, $\mathbf{G}$ and $\hat{\mathbf{G}}$, are used to map environmental and navigation process noise characterized by $\mathbf{Q}$ and $\hat{\mathbf{Q}}$, into $\mathbf{C}$ and $\hat{\mathbf{P}}$.

The measurement update equations for augmented and navigation state covariance matrices, $\mathbf{C}$ and $\hat{\mathbf{P}}$, at a measurement time $t_i$ are

$$\mathbf{C}^+(t_i) = \mathbf{A}\mathbf{C}^-(t_i)\mathbf{A}^T + \mathbf{B}\mathbf{R}^j(t_i)\mathbf{B}^T \tag{10}$$

$$\hat{\mathbf{P}}^+(t_i) = \left[\hat{\mathbf{I}} - \hat{\mathbf{K}}^j(t_i)\hat{\mathbf{H}}^j\right]\hat{\mathbf{P}}^-(t_i)\left[I - \hat{\mathbf{K}}^j(t_i)\hat{\mathbf{H}}^j\right]^T + \hat{\mathbf{K}}^j(t_i)\hat{\mathbf{R}}^j(t_i)\hat{\mathbf{K}}^j(t_i)^T \tag{11}$$

where the superscript '$j$' denotes the $j$th measurement type. The matrices $\mathbf{A}$ and $\mathbf{B}$ map the effects of the measurements and their associated noise to the navigation state dispersions. The Kalman gain is written as

$$\hat{\mathbf{K}}^j(t_i) = \hat{\mathbf{P}}(t_i)(\hat{\mathbf{H}}^j)^T\left[\hat{\mathbf{H}}^j\hat{\mathbf{P}}^-(t_i)(\hat{\mathbf{H}}^j)^T + \hat{\mathbf{R}}^j(t_i)\right]^{-1} \tag{12}$$

where the matrices $\hat{\mathbf{H}}$ and $\hat{\mathbf{R}}$ are the measurement sensitivity and measurement noise matrices, respectively.

The correction equations for $\mathbf{C}$ and $\hat{\mathbf{P}}$ at a maneuver time $t_m$ are

$$\mathbf{C}^+(t_m) = \mathbf{M}\mathbf{C}^-(t_m)\mathbf{M}^T + \mathbf{N}\boldsymbol{Q}_w^{act}\mathbf{N}^T \tag{13}$$

$$\hat{\mathbf{P}}^+(t_m) = \left[\hat{\mathbf{I}} + \hat{\mathbf{M}}\right]\hat{\mathbf{P}}^-(t_m)\left[I + \hat{\mathbf{M}}\right]^T + \hat{\mathbf{N}}\hat{\mathbf{Q}}_w^{act}\hat{\mathbf{N}}^T \tag{14}$$

The matrices $\mathbf{M}$ and $\hat{\mathbf{M}}$ contain the control partials associated with a linearized two-impulse targeting algorithm. The matrices $\mathbf{N}$ and $\hat{\mathbf{N}}$ are used to map the effects of actuator noise, described by $\boldsymbol{Q}_w^{act}$ and $\hat{\mathbf{Q}}_w^{act}$, into $\mathbf{C}$ and $\hat{\mathbf{P}}$.

**Trajectory Constraints and Metrics**

The baseline rendezvous maneuver profile contains 3 burns labeled Maneuver 1 (M1), Maneuver 2 (M2), and Maneuver 3 (M3) as shown in Figure 5. The trajectory constraints are driven by safety, crew schedule, desired final uncertainty, ground tracking performance, sensor requirements, and available propellant. To ensure a safe rendezvous with the target vehicle, this analysis ensures passive safety with a free drift and underburn constraint to guarantee that the chaser vehicle will not enter the approach sphere (before permission is granted after M3) or the keep-out sphere if the thrusters fail mid-burn or mid-transfer. The $3\sigma$ position dispersion from the nominal trajectory at M3 is the performance metric to quantify the GN&C system's uncertainty at the end of the profile. A high position dispersion indicates greater uncertainty of the chaser vehicle's position at M3 and implies poor performance. The constraints on time are driven by crew schedule and are a requirement of at least 1 hour between maneuvers and a restriction on additional time from the baseline profile's duration. In this scenario, a maximum of 3 hours to generate observability is the desired upper limit because any additional time poses a great demand on crew schedule. Also, in this notional scenario, the desired upper limit for allowable position dispersions at M3 are 1 km given the short distance to the target. The initial state dispersions in position and velocity are a function of ground site tracking performance. The $\pm 20$ deg approach corridor is to allow optical sensors and crew to visual acquire and track the target throughout the rendezvous and satisfy other vehicle system constraints. Finally, the available propellant constrains the change in velocity ($\Delta$v) allotted to perform maneuvers in this phase of flight. Time and nominal $\Delta$v are negatively correlated because lower maneuver $\Delta$v is generally associated with longer transfer times.

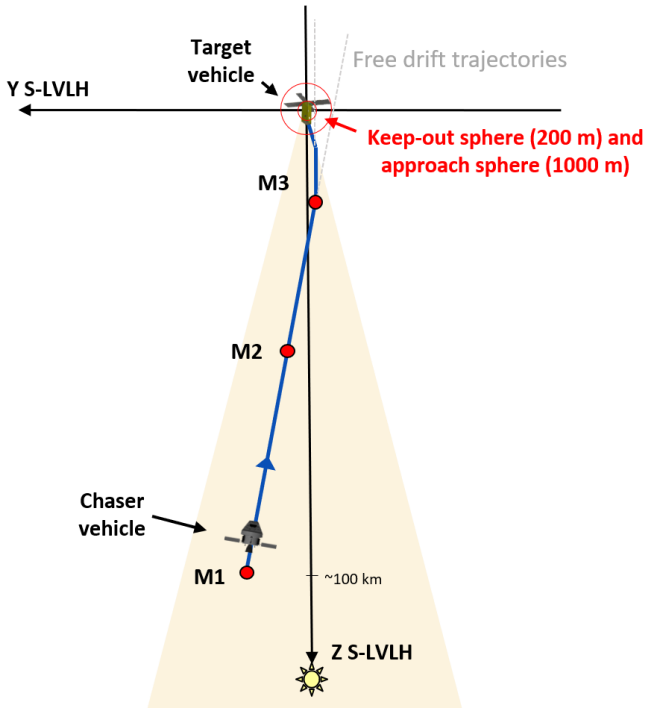


**Figure 5**: Direct-approach baseline NRHO rendezvous profile

### Cost Function

The cost function calculates total $\Delta$v (nominal $\Delta$v + $3\sigma_{\Delta \mathrm{v}_i}$) across all thruster burns including the 3 burns to maneuver from M1 to M3 in the baseline profile and the number of additional observability maneuvers ($n_{obs}$). Trajectory safety constraints are enforced using large penalties $\kappa$ added to the cost function when a constraint is violated. Thus, the optimization is set up to prioritize safety before propellant efficiency.

$$\text{cost} = \sum_{i=1}^{3+n_{obs}} (\Delta \mathrm{v}(\mathrm{t}_i) + 3\sigma_{\Delta \mathrm{v}_i}) + \kappa_{\text{approach corridor}} + \kappa_{\text{free drift}} + \kappa_{\text{transfer time}} \tag{15}$$

The trajectory constraints that are enforced by penalty are defined below. Notably, underburn (passive safety protection in case thrusters fail mid-burn) is not enforced by penalty and instead will be forced using out of plane geometry as described in a later section to reduce computation time.

*Approach Corridor* The approach corridor constraint requires nominal trajectories and associated $3\sigma$ position dispersions to stay within a $\pm 20^o$ cone around the z-axis behind the target vehicle in the Sun-referenced LVLH coordinate frame to satisfy operational requirements.

$$\kappa_{\text{approach corridor}} = \begin{cases} 10000 & \text{if } |\frac{y}{z}| > \tan(20^o) \text{ for any y, z on the } 3\sigma \text{ position ellipses} \\ 10000 & \text{if } |\frac{x}{z}| > \tan(20^o) \text{ for any x, z on the } 3\sigma \text{ position ellipses} \\ 0 & \text{otherwise} \end{cases} \tag{16}$$

*Free Drift* The free drift constraint requires that if the thrusters fail after a burn, the nominal state with $3\sigma$ dispersions for the associated free-drift trajectories will not encroach a 1 km approach sphere around the target vehicle for the M1, M2, and observability (OBS) burns and a 200 m keep-out sphere around the target vehicle for the M3 burn.

$$\kappa_{\text{free drift}} = \begin{cases} 10000 & \text{if } \rho - 3\sigma_\rho < \begin{cases} 1000 \text{ m} & \text{for the M1, M2, or OBS burns} \\ 200 \text{ m} & \text{for the M3 burn} \end{cases} \\ 0 & \text{otherwise} \end{cases} \tag{17}$$

*Maneuver Transfer Time* The maneuver transfer time constraint requires at least one hour between burns. This permits enough time for attitude adjustments and state measurements between maneuvers and would give a crew time to prepare between burns.

$$\kappa_{\text{transfer time}} = \begin{cases} 10000 & \text{if for burn times } t_i,\ \min_i(t_{i+1} - t_i) < 3600sec \\ 0 & \text{otherwise} \end{cases} \tag{18}$$

### Optimization Algorithm

The algorithms used to solve the angles-only optimization problem is a particle swarm optimizer (PSO) combined with a direct search algorithm developed by Goulet.[6] This dual approach allows the PSO to perform a global optimization search of the rather complex system and discontinuous nature of the cost functions. Once the PSO converges, the direct search algorithm continues the optimization process with just a few cost function evaluations to ensure the optimized solution is at least a local minimum. During each iteration, candidate values of the optimization variables are passed to the LinCov simulation, which passes results into a cost function and then returns the cost value to the optimizer. This process is illustrated in Figure 6.

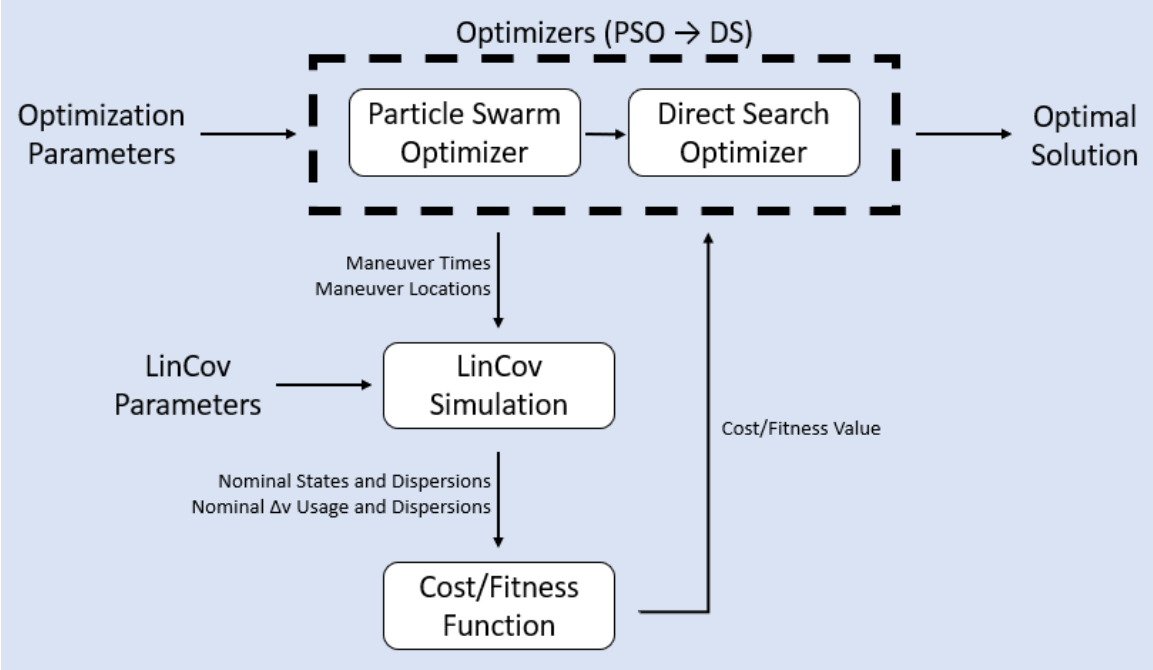


**Figure 6**: Functional relationship between the LinCov simulation and optimizers[6]

For all of the results presented in the sections below, each trajectory optimization used 400 particles and 300 iterations in the particle swarm optimizer. For a 17 core computer cluster, each optimization took approximately 3 hours, which corresponds to a wall clock time of about 1.5 seconds per particle (trajectory) evaluation. In comparison to the PSO run time, the direct search algorithm added a trivial duration to total run time (usually 1 to 2 minutes). The results from 35 simulations are presented below with a total simulation time of approximately 110 hours.

## GN&C MODELING

### Reference Frames

As summarized by Mand,[3] the reference frames that describe the inertial and relative rendezvous trajectories are illustrated in Figure 7. The Earth-Centered inertial reference frame has its origin at the center of

Earth with the primary x-axis fixed, pointed at the vernal equinox, and the z-axis aligned with the rotation axis of Earth at a specific epoch defined as noon on January 1st, 2000 as the J2000 frame. The bottom-right picture displays the Earth-Moon rotating pulsating frame (EM) where the x-axis is pointed from the Earth to the Moon and the z-axis is perpendicular to the Moon's orbital plane. Notably, the distance between the Earth and Moon is normalized to the mean value such that the frame is pulsating.

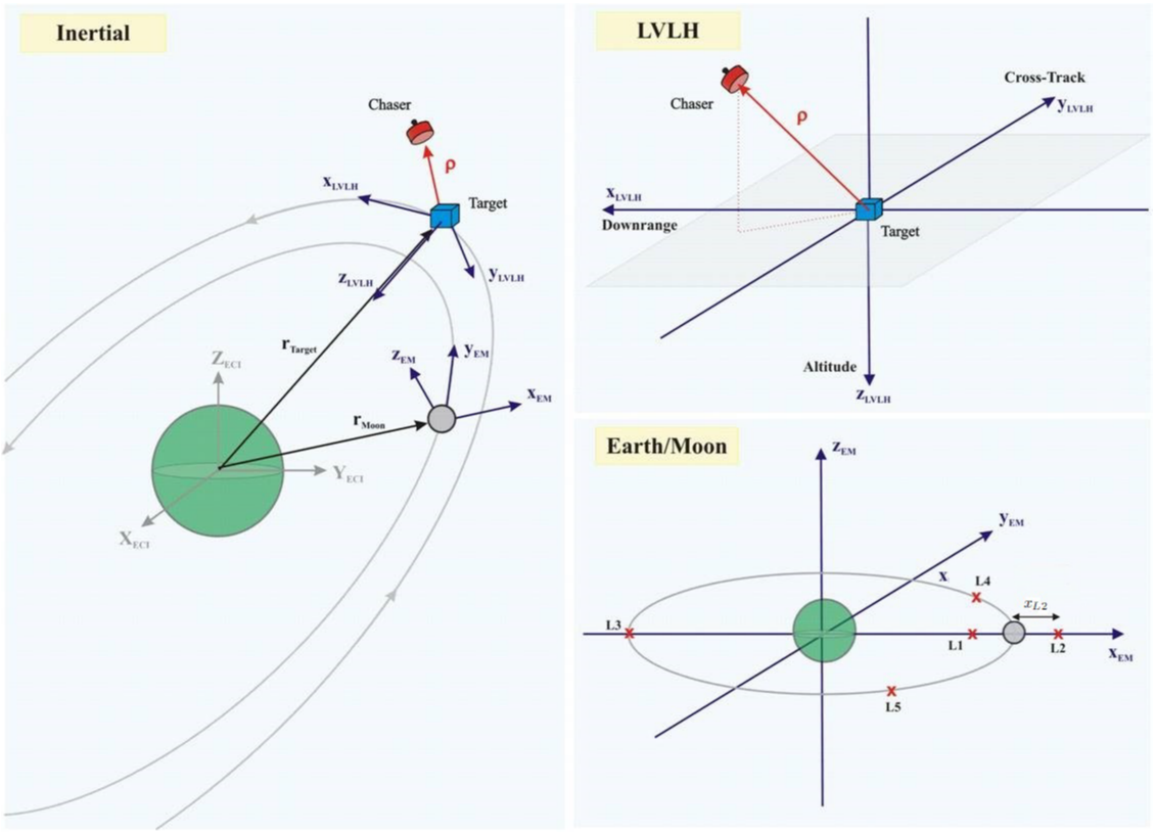


**Figure 7**: Inertial, LVLH, and Earth-Moon rotating reference frames

Conventionally, relative trajectories for rendezvous in a low Earth/lunar orbit are described using the local vertical, local horizontal (LVLH) frame with its origin at the target vehicle. The x-axis (downrange) is generally pointed in the direction of target velocity and the z-axis (altitude) is aligned with the radial vector to the central body being orbited. However, for an NRHO, the velocity vector would not be generally aligned with the x-axis. Additionally, in this case, operational constraints require that the chaser vehicle approaches the target with the sun at a specific angle. Thus, this analysis uses the Sun-referenced LVLH frame (S-LVLH) with the direction to the sun aligned with the z-axis and the negative y-axis generally pointing near the Moon for most of the orbital period. Figure 8 presents the S-LVLH frame.

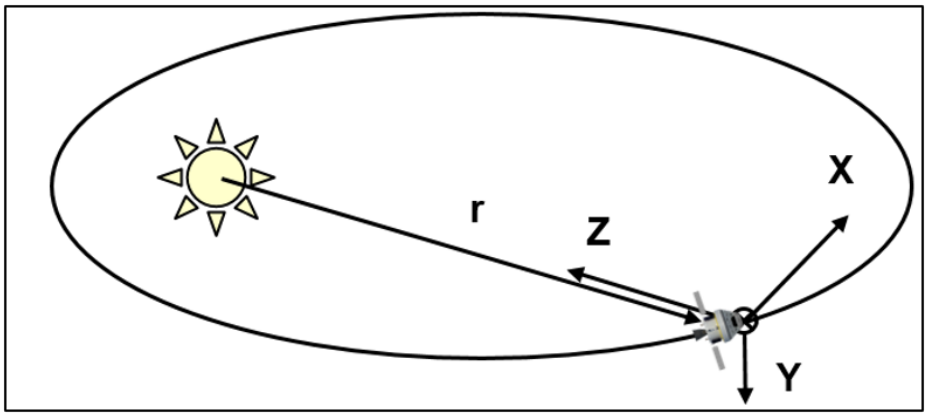


**Figure 8**: Sun-referenced LVLH frame

**Linearized NRHO Dynamics**

The significant number of calculations made within the optimization process requires a simpler, lower fidelity dynamics model to reduce computation time. Luquette linearizes relative motion dynamics for the restricted three body problem (RTBP) about the target spacecraft in his doctoral dissertation *Nonlinear Control Design Techniques for Precision Formation Flying at Lagrange Points*. Assuming the rotation of the Sun-referenced LVLH coordinate frame is negligible, this is expressed as the system of differential equations

$$\dot{\mathrm{X}} = \begin{bmatrix} 0_3 & \mathbf{I}_3 \\ \Xi(\mathrm{t}) & 0_3 \end{bmatrix} \mathrm{X} = A_{LR}\mathrm{X} \tag{19}$$

where

$$\Xi(\mathrm{t}) = -\left(\frac{\mu_1}{|\mathbf{r}_{1L}|^3} + \frac{\mu_2}{|\mathbf{r}_{2L}|^3}\right)\mathbf{I}_3 + \frac{3\mu_1}{|\mathbf{r}_{1L}|^3}\left[\mathbf{e}_{1L}\cdot\mathbf{e}_{1L}^{\mathrm{T}}\right] + \frac{3\mu_2}{|\mathbf{r}_{2L}|^3}\left[\mathbf{e}_{2L}\cdot\mathbf{e}_{2L}^{\mathrm{T}}\right] \tag{20}$$

Figure 9 shows the vectors referenced in Equation 20: $\mathbf{r}_{1L}$ and $\mathbf{r}_{2L}$ refer to the vectors from the two central masses to the leader (target) satellite, whereas $\mathbf{e}_{1L}$ and $\mathbf{e}_{2L}$ refer to the normalized form of these vectors. $\mu_1$ and $\mu_2$ represent the gravitational parameters of the two central masses. In this paper, the two central masses are the Earth and the Moon. Assignment of the "1" and "2" subscripts to these bodies is arbitrary.

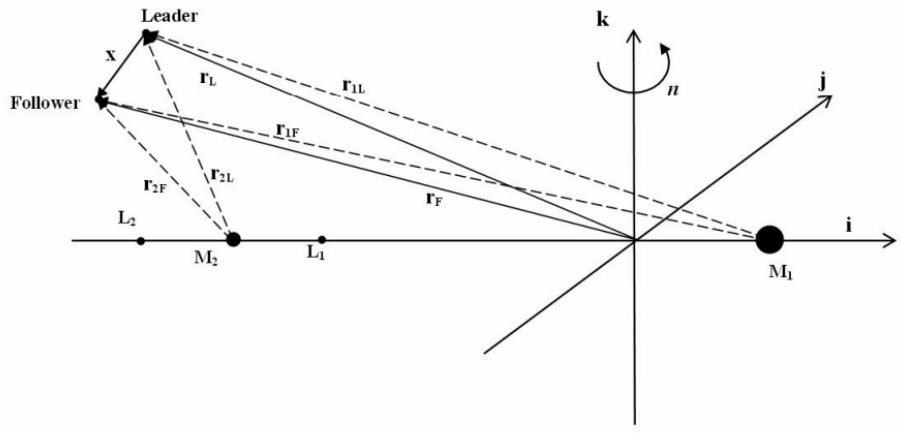


**Figure 9**: Diagram of vectors in the RTBP

### Linearized Relative Targeting

Deriving the targeting equation for linear relative dynamics requires the system's state transition matrix (STM). Though $\mathbf{A}_{\text{LR}}$ varies with time, this change is negligible for sufficiently small differences in timesteps. For a given time $\text{t}_j$, the system's STM from $\text{t}_j$ to $\text{t}_j + \Delta\text{t}$ is given by

$$\Phi_j(\Delta\text{t}) = e^{\mathbf{A}_{\text{LR}}(\text{t}_j)\Delta\text{t}} \tag{21}$$

An approximate STM between distant timesteps may be formed via the product of intermediate STMs. Assuming a uniform $\delta$t between timesteps such that $\Delta\text{t} = n\delta\text{t}$,

$$\Phi(\Delta\text{t}) = \prod_{j=1}^{n} \Phi_j(\delta\text{t}) \tag{22}$$

Since there are six states in the current system (relative position and velocity vectors), $\Phi(\Delta\text{t})$ is a 6x6 matrix. Thus, it can be broken into four 3x3 components:

$$\Phi(\Delta\text{t}) = \begin{bmatrix} \Phi_{rr} & \Phi_{rv} \\ \Phi_{vr} & \Phi_{vv} \end{bmatrix} \tag{23}$$

Using $\Phi(\Delta\text{t})$ to determine how an instantaneous change in velocity $\Delta\mathbf{v}$ will influence the relative position at time $\text{t}_i + \Delta\text{t}$,

$$\begin{bmatrix} \mathbf{r}_f \\ \mathbf{v}_f \end{bmatrix} = \begin{bmatrix} \Phi_{rr} & \Phi_{rv} \\ \Phi_{vr} & \Phi_{vv} \end{bmatrix} \begin{bmatrix} \mathbf{r}_i \\ \mathbf{v}_i + \Delta\mathbf{v} \end{bmatrix} \tag{24}$$

$$\mathbf{r}_f = \Phi_{rr}\mathbf{r}_i + \Phi_{rv}\left(\mathbf{v}_i + \Delta\mathbf{v}\right) \tag{25}$$

So, targeting a position $\mathbf{r}_f$ from a given state $[\mathbf{r}_i, \mathbf{v}_i]^{\text{T}}$ requires a $\Delta\mathbf{v}$ of

$$\Delta\mathbf{v}_{nominal} = \Phi_{rv}^{-1}\left(\mathbf{r}_f - \Phi_{rr}\mathbf{r}_i\right) - \mathbf{v}_i \tag{26}$$

In this simulation, there is $3\sigma$ thruster noise of 0.015 m/s. Thus, the actual $\Delta\mathbf{v}$ produced by a maneuver is given by

$$\Delta\mathbf{v}_{actual} = \Delta\mathbf{v}_{nominal} + \eta_{thruster} \tag{27}$$

### Sensor Models

The sensor measurements assumed for this study are the relative range, range-rate, and bearing angle between the chaser and target vehicle. To reduce the computational load, simplified models are adopted which are presented in Equations 28-30.

$$\mathbf{z}_\rho = |\mathbf{r}| + \eta_\rho \tag{28}$$

$$\mathbf{z}_{\dot{\rho}} = \mathbf{v}^T \frac{\mathbf{r}}{|\mathbf{r}|} + \eta_{\dot{\rho}} \tag{29}$$

$$\mathbf{z}_{los} = \frac{\mathbf{r}}{|\mathbf{r}|} + \eta_{los} \tag{30}$$

The $3\sigma$ noise for the bearing angle is $2 \cdot 10^{-4}$ rad in both the azimuth and elevation directions. The $3\sigma$ dispersions for range and range-rate are 25 m and 0.25 m/s respectively in all directions.

## ROBUST TRAJECTORY DESIGN FOR ANGLES ONLY NAVIGATION IN NRHO

This section begins by comparing the performance of a given GN&C system in following a baseline trajectory with a sensor suite that provides range, range-rate, and angle measurements to an onboard navigation filter. Then, this section illustrates the necessity of chaser vehicle maneuvers to sufficiently reduce navigation uncertainties to enable an angles-only rendezvous. The objective of these results is to provide insight into the feasibility of performing a robust optimization of an angles-only NRHO rendezvous and the costs of trades in trajectory constraints to achieve desired performance.

### Baseline Rendezvous Trajectory

As shown in Figure 10, the baseline maneuver profile contains 3 burns (M1, M2, and M3) beginning on the positive Y and Z S-LVLH axes at M1 and ending on the negative y-axis at M3. The M1 initiation point is 100 km from M3 and is preceded by a 1 hour period for target acquisition and preparation for the rendezvous sequence. The M2 burn is a mid-course correction and has zero $\Delta$v nominally. The shaded part of Figure 10 represents the $\pm 20^o$ cone of the approach corridor.

Table 1 below describes the assumed sensor error values, thruster errors, process noise, initial dispersions, and initial navigation errors for the LinCov analysis.

**Table 1**: Uncertainty parameters for LinCov analysis

| Description | Value | Units |
|---|---|---|
| Initial position dispersions ($3\sigma$) | $[7.75, 7.75, 7.75]$ | km |
| Initial velocity dispersions ($3\sigma$) | $[1.55, 1.55, 1.55]$ | m/s |
| Initial navigation position error ($3\sigma$) | $[7.75, 7.75, 7.75]$ | km |
| Initial navigation velocity error ($3\sigma$) | $[1.55, 1.55, 1.55]$ | m/s |
| Process noise dispersion and error | $[5 \times 10^{-8}, 5 \times 10^{-8}, 5 \times 10^{-8}]$ | $m^2/s^3$ |
| Thruster noise dispersion and error ($3\sigma$) | $[15, 15, 15]$ | mm/s |

### Comparison of Full Sensor Suite and Angles-Only Navigation on Baseline Trajectory

The chaser vehicle's baseline relative navigation sensor suite includes range and range-rate measurements along with bearing or angle measurements. However, the sensor suite in this contingency scenario relies solely on angle measurements. Figures 11a and 11b illustrate the position dispersions from a LinCov analysis for the integrated GN&C performance of the chaser vehicle along the direct-approach baseline trajectory

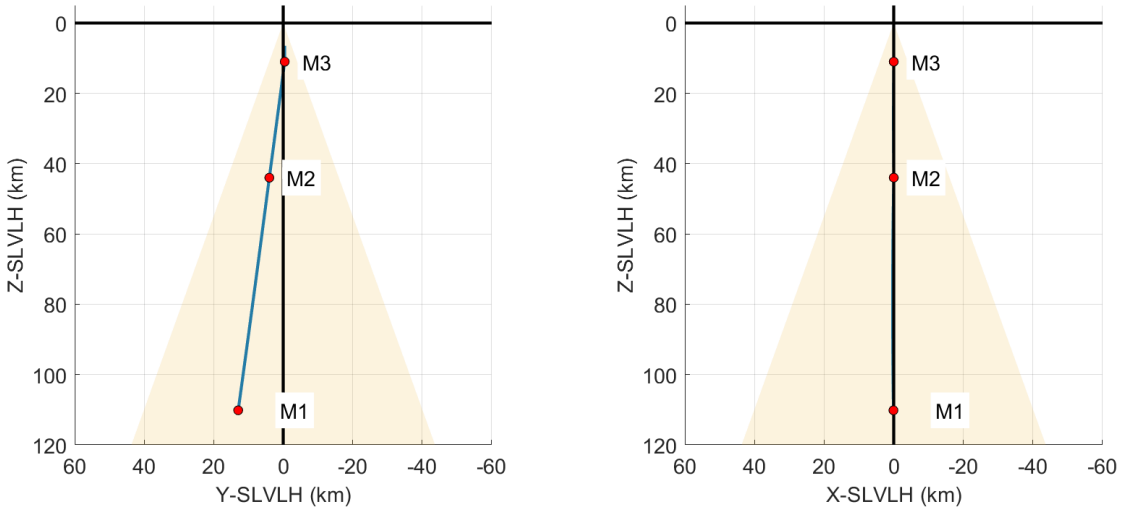


(a) Baseline in-plane

(b) Baseline out-of-plane

**Figure 10**: Baseline NRHO rendezvous trajectory

with range, range-rate, and angle measurements. Figures 11c and 11d illustrate the position dispersions with angles-only navigation. By inspection, the plots of the angles-only navigation case have elongated position dispersion ellipses in the line-of-sight direction.

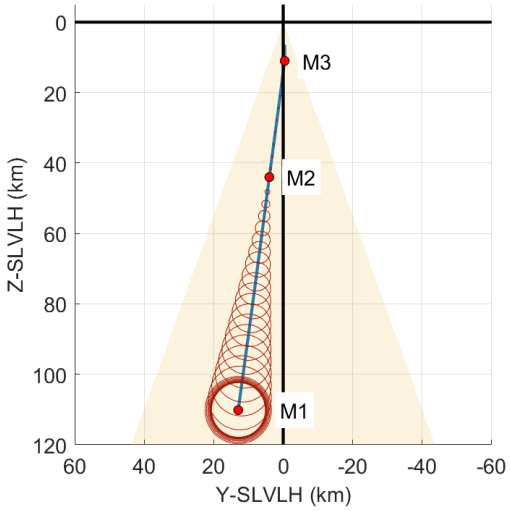


(a) In-plane: range + range-rate + angles

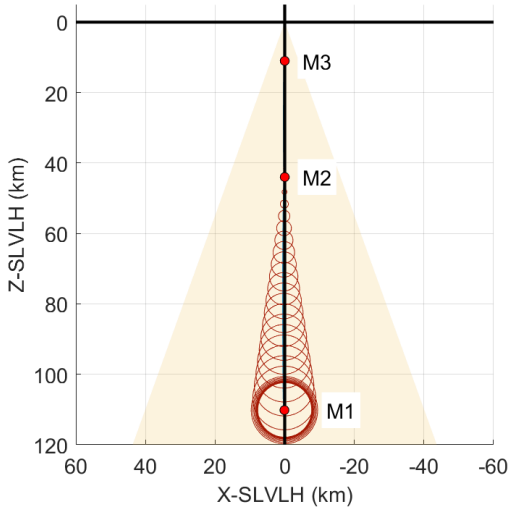


(b) Out-of-plane: range + range-rate + angles

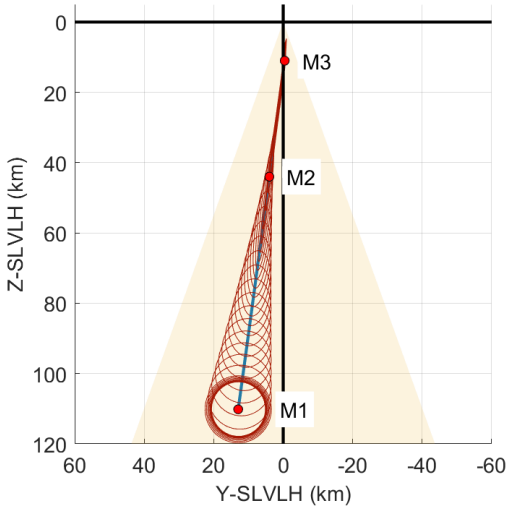


(c) In-plane: angles-only

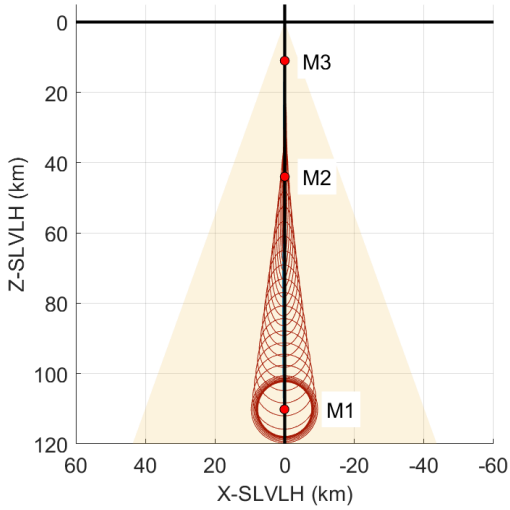


(d) Out-of-plane: angles-only

**Figure 11**: Baseline trajectory: sensor suite comparison

The performance values provided in Table 2 indicate that the angles-only case arrives at the M3 burn with a navigation position error that is 77.33 times greater and position dispersions that are 25.38 times greater than the value in the range + range-rate + angles case. This demonstrates that the lack of range observability in the angles-only case creates significant uncertainties in the navigation filter, which lead to significant position dispersions from the desired M3 location due to the GN&C system's inability to accurately follow the reference trajectory.

**Table 2**: Baseline trajectory: Range + Range-rate + Angles vs Angles-only

| Sensor Suite | Nominal $\Delta$v (m/s) | Total $\Delta$v (m/s) | M3 Position Dispersion (m) | M3 Navigation Position Error (m) |
|---|---|---|---|---|
| Range + Range-rate + Angles | 12.49 | 19.377 | 248.8 | 7.3 |
| Angles-only | 12.49 | 30.082 | 6314.4 | 564.5 |

To highlight the difference in GN&C performance between the baseline navigation sensors and the angles-only case between the previous scenarios, Figure 12 presents a summary of the relative position and velocity statistics (environmental dispersions and true navigation error) in each S-LVLH axis for the full sensor suite case (range + range-rate + angles). As expected, the navigation error rapidly decreases from the initial values indicating that the sensor measurements have reduced the navigation filter's uncertainty in position and velocity. After the first maneuver (M1), the position environment dispersions decrease due to the GN&C system correcting the vehicle back to the desired reference trajectory. Since the GN&C system has low navigation uncertainty in this case, the maneuvers are successful in reducing the environmental dispersions.

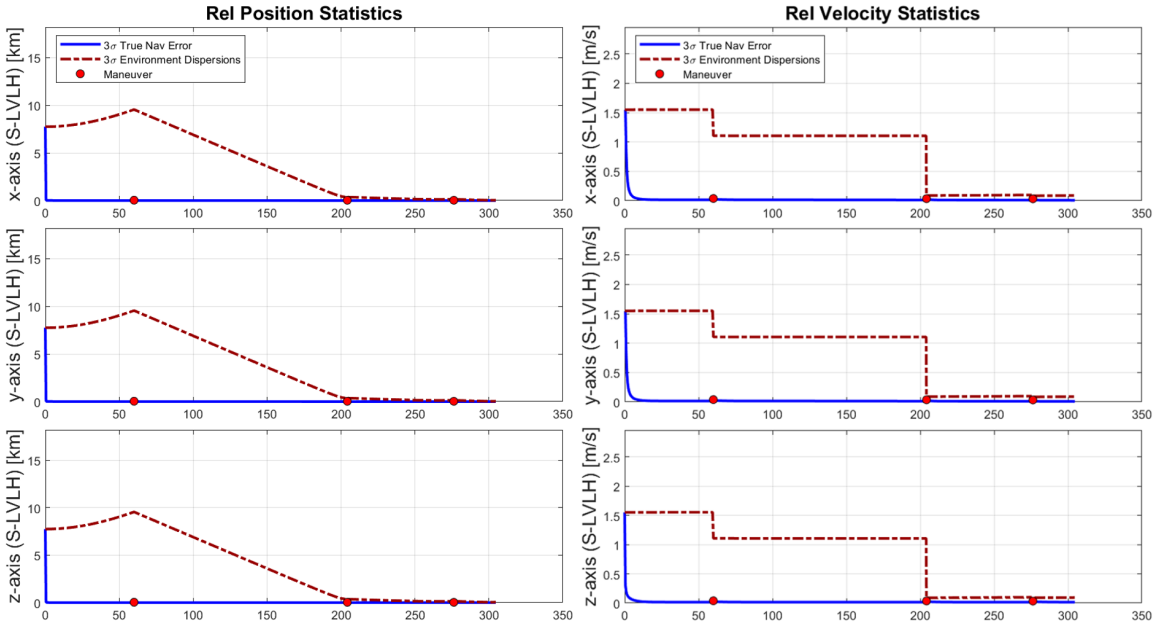


**Figure 12**: Relative dispersion and error summary for baseline trajectory with Range + Range-rate + Angles

However, in the case of the baseline maneuver profile with only angle measurements, Figure 13 illustrates the significant navigation uncertainties in the line-of-sight direction (mostly along the z-axis in the S-LVLH frame). Unlike in the x-axis and y-axis, the navigation uncertainties do not rapidly approach zero in the z-axis from their initial values as shown in the bottom two plots in Figure 13. Due to the high navigation uncertainties in range, the M1 maneuver is unable to correct the environmental dispersions, which allows significant growth in position dispersions as the chaser vehicle approaches the target. Thus, the apparent lack of range observability is the cause of the M3 position dispersions being 25.38 times greater in the angles-only case. Notably, the navigation errors in the z-axis eventually decrease because M1 is a known chaser vehicle maneuver with a small velocity component perpendicular to the chaser's line-of-sight to the target. However,

despite the navigation error eventually converging, the position dispersions are too high at M3 to allow for a safe rendezvous. Thus, the baseline trajectory profile must be modified to permit an angles-only rendezvous by adding maneuvers that generate sufficient observability.

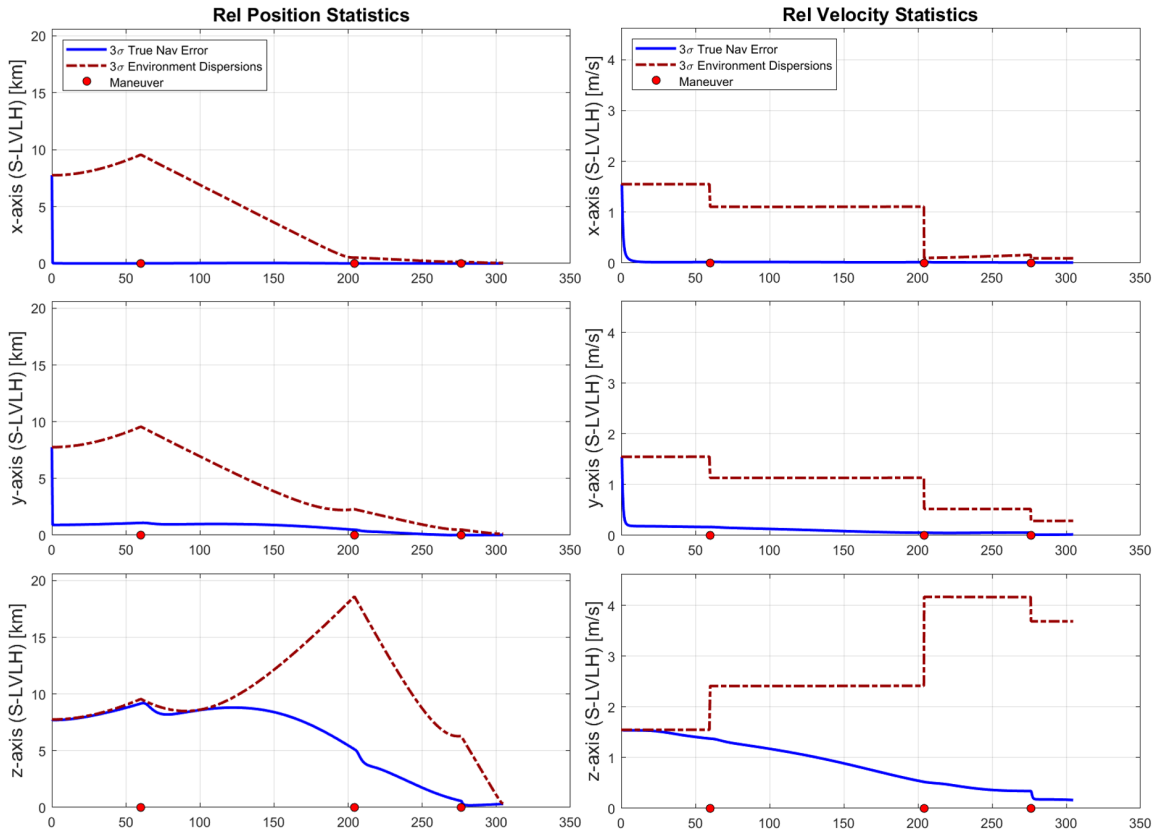


**Figure 13**: Relative dispersion and error summary for baseline trajectory with angles-only navigation

### Observability Maneuvers

A system is observable if the initial state can be determined from the inputs and outputs,[16] which are translational maneuvers and sensor measurements in this problem. Previously, Woffinden analytically demonstrated that for a linear time-invariant system (including linear relative orbital motion dynamics), angles-only measurements are insufficient for determining the initial relative position and velocity.[11] He shows that the relative range to a chaser vehicle is unobservable for linear relative orbital dynamics despite relative natural motion and that observability is guaranteed when the change in position due to a calibrated thrust acceleration is not aligned with the natural line-of-sight profile. A linear covariance analysis of angles-only relative motion from Chari[10] indicates that relative natural motion with a component normal to the line-of-sight will eventually reduce the range uncertainty due to nonlinearities in the orbital dynamics. However, his analysis indicates that relative orbital motion alone, which relies on natural motion is often not sufficient to reduce the range uncertainty to an acceptable level for proximity operations in low earth orbit. As shown in the previous section, this observability problem persists in the case of linearized NRHO relative dynamics around the moon. Thus, there is a need for chaser vehicle observability maneuvers to decrease range uncertainty. While previous work indicates that the ideal observability maneuver is completely perpendicular to the line-of-sight, such maneuvers require greater deviations from the baseline trajectory and more $\Delta$v. Thus, the optimization problem asks where and when to place additional observability maneuvers in the baseline trajectory to mini-

mize the total ($3\sigma$ + nominal) $\Delta$v usage while adhering to operational and safety constraints included a cost function.

In the presented scenario of a hypothetical angles-only contingency after lunar departure, the baseline NRHO rendezvous trajectory will be modified by inserting observability maneuvers between M1 and M2. The baseline profile between M2 and M3 will be preserved. This analysis will assume that due to mission constraints, a desirable baseline for a maneuver-assisted trajectory would add up to an additional 3 hours and 20 m/s of $\Delta$v to the direct-approach baseline profile to generate observability and limit the allowable $3\sigma$ position dispersion at M3 to 1 km. These constraints are attributed to crew schedule, available propellant, and allowable risk (where a higher M3 $3\sigma$ position dispersion implies greater risks of collision). Finally, the observability maneuvers will be selected out-of-plane of the baseline direct-approach trajectory to preserve the in-plane nominal profile between M1 and M3 and to ensure that the underburn constraint is met. As seen in Figure 14, most locations for observability burns in-plane with the baseline trajectory would violate the underburn constraint, which prevents a collision due to thruster failures mid-burn. Thus, selecting observability maneuver locations on the x-axis while maintaining the in-plane baseline profile ensures that the underburn constraint is fulfilled.

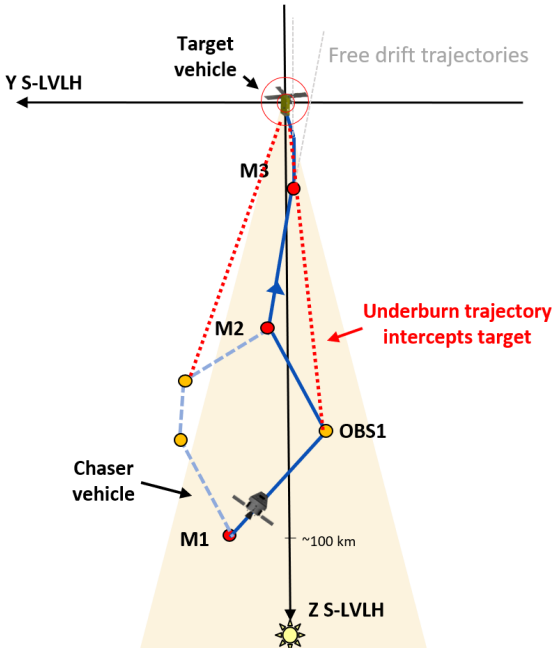


**Figure 14**: Illustration of underburn conflict with in-plane observability maneuvers

The optimizer minimizes the cost function for minimum total $\Delta$v ($3\sigma$ + nominal) by choosing the following variables for each observation burn (OBS burn): x-axis burn location, z-axis burn location, and burn time. The following sections present the results of this optimization problem while highlighting sensitivities in the trade space. Each section will present a plot with each point describing a minimum $\Delta$v optimized trajectory to show variations in trajectory parameters and the associated increase in total $\Delta$v (nominal + $3\sigma$) from the baseline trajectory. Each section also compares the GN&C statistics and dispersion plots of the previously described baseline observability maneuver-assisted trajectory (additional 3 hours and 1 km allowable M3 $3\sigma$ position dispersion) with an "improved" maneuver-assisted trajectory based on potentially desirable engineering trades.

### Variation of burn number with additional time

The baseline direct-approach trajectory has a total transfer time of 4.6 hours from M1 to M3. For this hypothetical angles-only scenario, additional time to generate observability is unfavorable for the crew's schedule. Thus, the aforementioned desired maneuver-assisted baseline limits the additional time to 3 hours. In this section, the additional time for observability maneuvers between M1 and M2 is varied with the number of observability burns to find desirable engineering trades between additional time and additional $\Delta$v usage. From this analysis, a single observability burn results in the lowest additional $\Delta$v from the direct-approach baseline trajectory. Thus, the baseline maneuver-assisted trajectory is limited to one observability burn, 3 additional hours, and a 1 km allowable position dispersion. Since a lower total $\Delta$v usage is highly desirable and would likely outweigh minor impacts on crew schedule, the chosen "improved" trajectory adds 2 more hours from the maneuver-assisted baseline for a 1.98 m/s reduction in total $\Delta$v as shown in Table 3.

**Table 3**: Comparison of variation in burn number and additional time from baseline

| Case | OBS burn number | Additional time (hrs) | Additional total $\Delta$v (m/s) from baseline profile | M3 Position Dispersion (m) | M3 Navigation Position Error (m) |
|---|---|---|---|---|---|
| Baseline maneuver-assisted | 1 | 3 | 10.898 | 1000.0 | 252.2 |
| Improved | 2 | 5 | 8.913 | 1000.0 | 256.4 |

Figure 15a presents a summary of the variations in additional time and observability burn number. Intuitively, additional time would be expected to reduce the total $\Delta$v because longer transfer times have smaller velocities. However, as shown in the summary plot, additional time is only shown to reduce total $\Delta$v in the trajectories with 2 or 3 observability burns. This is because the single observability burn case is limited by the approach corridor since the chaser vehicle must drift in a single direction for the longest distance compared to the 2 and 3 OBS burn cases. To prevent the $3\sigma$ position dispersions from exiting the approach corridor, the optimizer is limited to trajectories that are less $\Delta$v efficient for increasing values of additional time. This results in the total $\Delta$v increasing with additional time for the 1 OBS burn case after approximately 3 additional hours. Figures 15b and 15c are plots of the baseline 1 OBS burn maneuver-assisted trajectory and Figures 15d and 15e are plots of the 2 OBS burn "improved" trajectory.

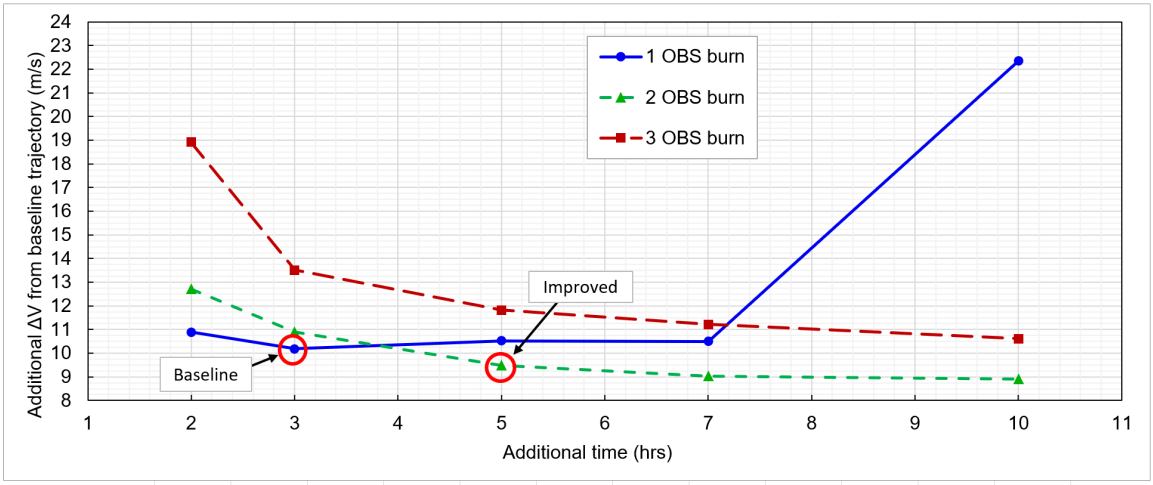


(a) Minimum $\Delta$v optimized trajectory variations in burn number and additional time

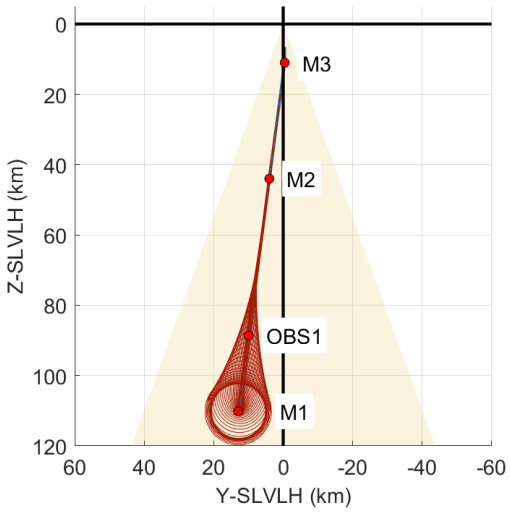


(b) In-plane: baseline maneuver-assisted

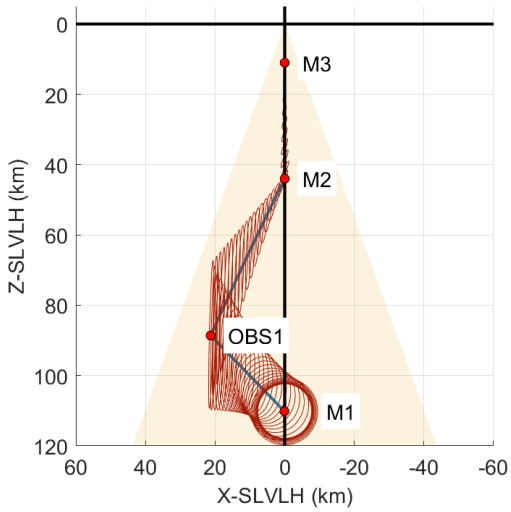


(c) Out-of-plane: baseline maneuver-assisted

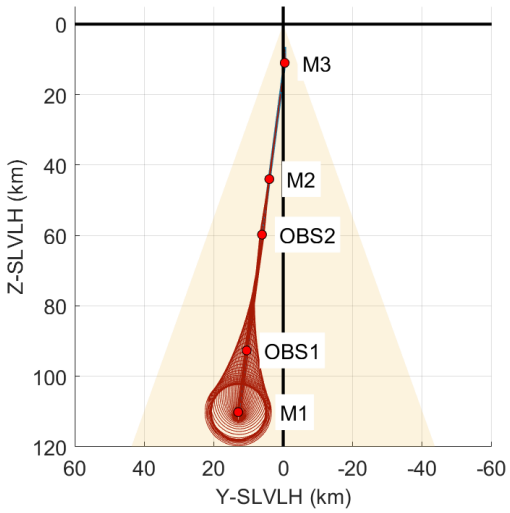


(d) In-plane: improved maneuver-assisted

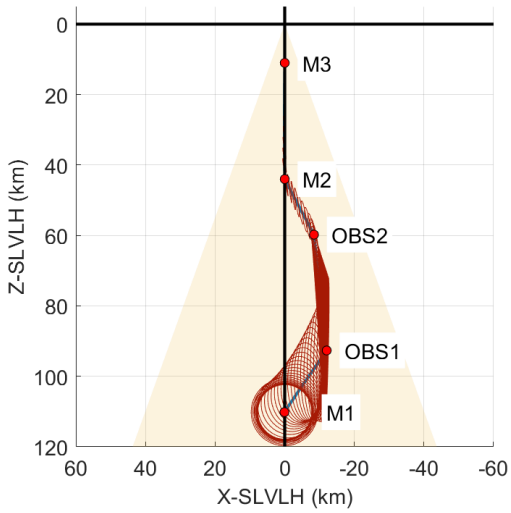


(e) Out-of-plane: improved maneuver-assisted

**Figure 15**: Variation in burn number and additional time

### Variation of burn number and position uncertainty at M3

As mentioned, the baseline maneuver-assisted trajectory has a 1 km allowable $3\sigma$ position dispersion limit at M3 because higher position dispersion values, which are a metric for state uncertainty, imply a greater risk for a successful rendezvous. Thus, for this scenario of a crewed cislunar rendezvous, it is assumed a smaller allowable position dispersion would outweigh minor increases in $\Delta$v usage. As such, the chosen "improved" trajectory reduces the limit on allowable M3 $3\sigma$ position dispersions to 700 m for a 2.35 m/s increase in total $\Delta$v from the maneuver-assisted baseline as shown in Table 4.

**Table 4**: Comparison of variation in burn number and allowable $3\sigma$ M3 position dispersions from baseline

| Case | OBS burn number | Allowable position dispersion (m) | Additional total $\Delta$v (m/s) from baseline profile | M3 Position Dispersion (m) | M3 Navigation Position Error (m) |
|---|---|---|---|---|---|
| Baseline maneuver-assisted | 1 | 1000 | 10.898 | 1000.0 | 252.2 |
| Improved | 2 | 700 | 13.249 | 700.0 | 232.8 |

Figure 16a presents a summary of the variations in allowable position dispersions and observability burn number. As expected, looser position dispersion requirements (higher value) require smaller observability maneuvers to generate observability and thus less total $\Delta$v. This is indicated by the summary plot, which shows that higher values of allowable M3 position dispersions consistently reduce total $\Delta$v across 1, 2, and 3 OBS burn cases. The summary plot also indicates that for a 1 km allowable M3 dispersion, the 1 and 2 OBS burn trajectories have similar deltav usage. However, for smaller (tighter) allowable position dispersions, the 2 OBS burn case uses the least total deltaV. Thus, the "improved" trajectory uses 2 OBS burns for a tighter position dispersion requirement. Figures 16b and 16c are plots of the baseline 1 OBS burn maneuver-assisted trajectory and Figures 16e and 16e are plots of the 2 OBS burn "improved" trajectory.

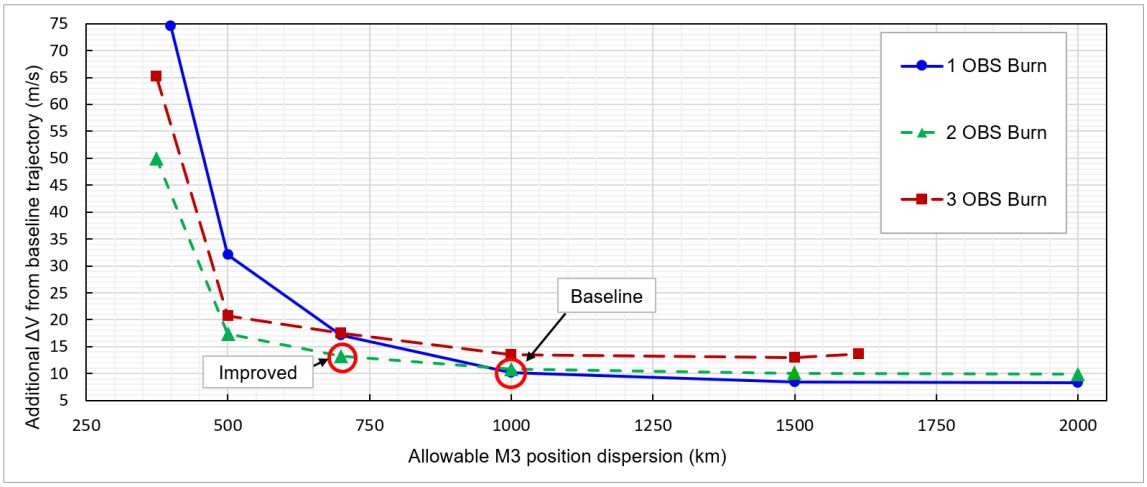


(a) Minimum $\Delta$v optimized trajectory variations in burn number and allowable position dispersion

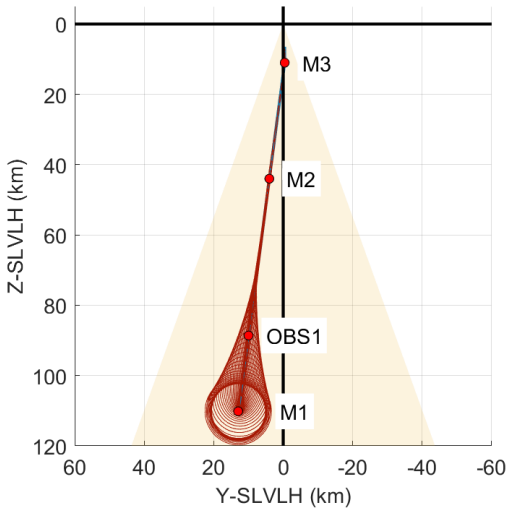


(b) In-plane: baseline maneuver-assisted

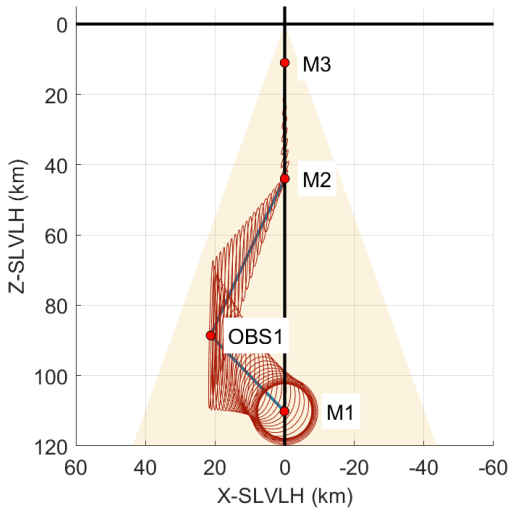


(c) Out-of-plane: baseline maneuver-assisted

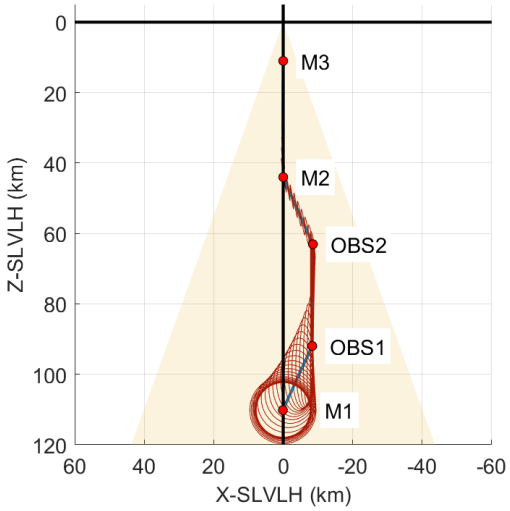


(d) In-plane: baseline maneuver-assisted

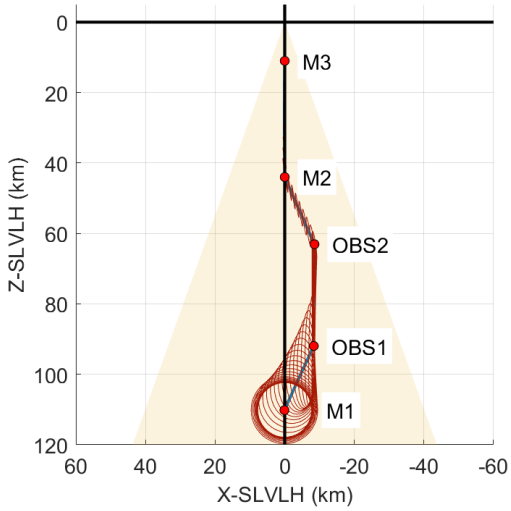


(e) Out-of-plane: improved maneuver-assisted

**Figure 16**: Variations in burn number and allowable M3 $3\sigma$ position dispersion

**Variation in burn number, initial navigation error, and initial state uncertainty**

The initial uncertainty parameters from Table 1 indicate an initial $3\sigma$ position dispersion and navigation error of 7.75 km and an initial $3\sigma$ velocity dispersion and navigation error of 1.55 m/s in all axes. For this notional scenario, the initial dispersions and navigation error at the beginning of the rendezvous are a function of the ground site tracking performance and the GN&C performance during the lunar departure and NRHO insertion before rendezvous. Thus, a scaling factor that decreases the initial dispersions and navigation error in this section represents better ground site tracking performance and better GN&C performance pre-rendezvous. In this scenario, a lower total $\Delta$v usage is assumed to outweigh the cost of achieving a smaller initial navigation error and state uncertainty. Accordingly, the "improved" maneuver-assisted trajectory scales the initial errors and dispersions by 0.5 for a significant 3.808 m/s reduction in total $\Delta$v from the baseline maneuver-assisted trajectory as shown in Table 4.

**Table 5**: Comparison of variation in burn number and initial environmental dispersions/navigation errors from baseline

| Case | Burn number | Scale Factor to initial disp and nav error (m) | Additional total $\Delta$v (m/s) from baseline profile | M3 Position Dispersion (m) | M3 Navigation Position Error (m) |
|---|---|---|---|---|---|
| Baseline maneuver-assisted | 1 | 1.0 | 10.898 | 1000.0 | 252.2 |
| Improved | 1 | 0.5 | 7.090 | 1000.0 | 252.4 |

Figure 17a is a summary of the variations in initial navigation error, state dispersion, and OBS burn number. For all variations on OBS burn number, the total $\Delta$v decreased with smaller initial errors/dispersions. Since the trajectories with a single observability burn used the least total $\Delta$v for any given scale factor, both the baseline and "improved" maneuver-assisted trajectories use a single OBS burn. Figures 17b and 17c are plots of the baseline 1 OBS burn maneuver-assisted trajectory and Figures 17d and 17e are plots of the 2 OBS burn "improved" trajectory.

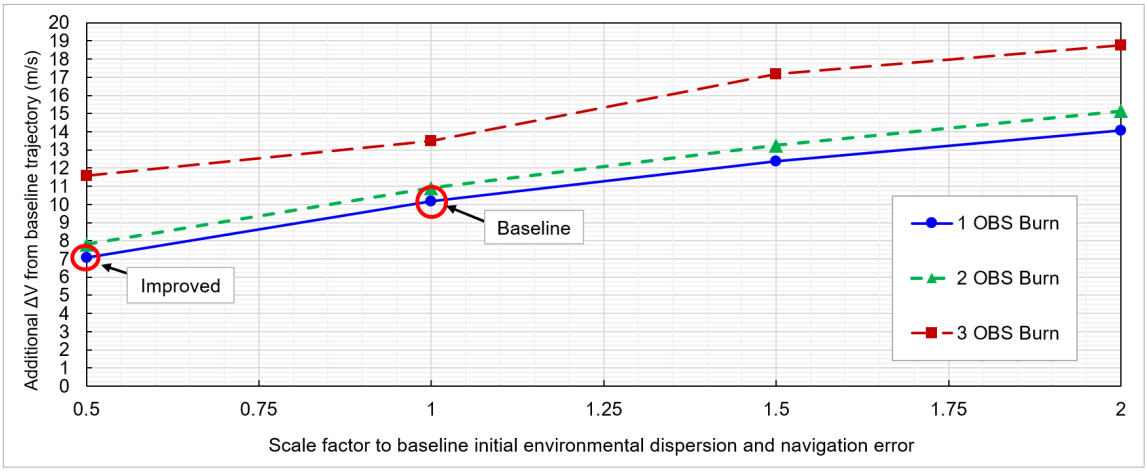


(a) Minimum $\Delta$v optimized trajectory variations

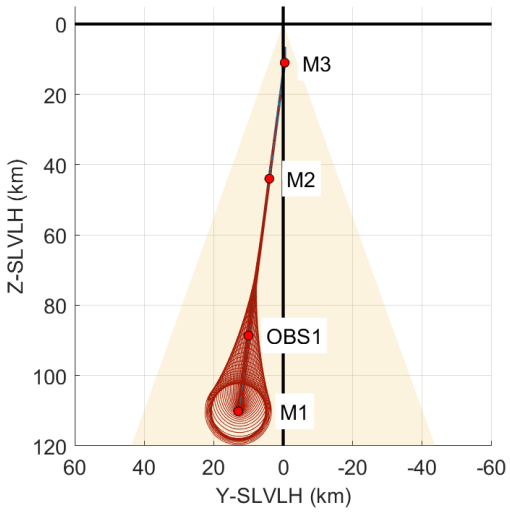


(b) In-plane: baseline maneuver-assisted

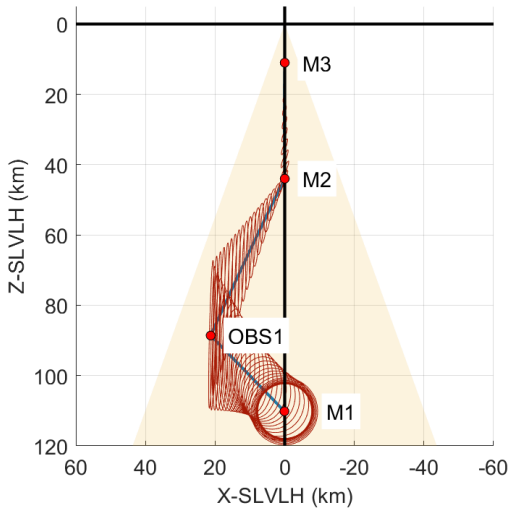


(c) Out-of-plane: baseline maneuver-assisted

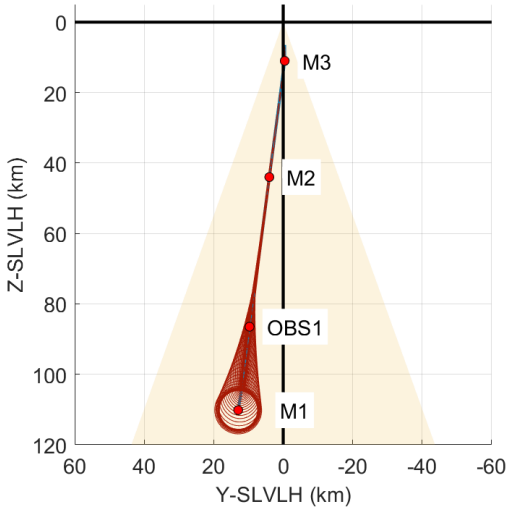


(d) In-plane: improved maneuver-assisted

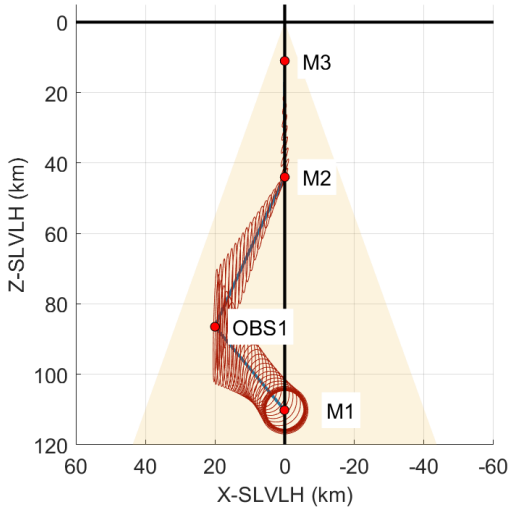


(e) Out-of-plane: improved maneuver-assisted

**Figure 17**: Variations in burn number and scale factor on initial environmental dispersions and navigation errors

## CONCLUSION

The objective of this paper was to demonstrate that a LinCov robust optimization method could be applied to angles-only rendezvous in an NRHO and to highlight the sensitivity to various trajectory constraints. The observability limitations of angles-only navigation result in significant navigation errors in the line-of-sight direction from a chaser vehicle to a target. Consequently, the state uncertainty of the chaser vehicle GN&C system is often too high to permit a safe rendezvous with angles-only navigation. Thus, calibrated chaser vehicle maneuvers are required to induce observability. In this analysis, an optimization algorithm is used to solve for the optimal times and locations for these observability maneuvers to minimize $\Delta$v while adhering to specific operational constraints expressed in a cost function. Since optimization algorithms such as the particle swarm optimizer in this analysis must evaluate the GN&C performance metrics for hundreds of

trajectory candidates, LinCov analysis is used to determine these metrics rapidly compared to conventional methods. By optimizing angles-only trajectories for an assortment of constraints, this work highlights the utility of a similar analysis to find desirable engineering trades. This study indicated that when generating observability in the notional crewed NRHO rendezvous scenario, a longer time duration does not necessarily result in smaller total $\Delta$v usage. In this case, the approach corridor (an operational constraint) made it such that the number of observability maneuvers had to increase to at least two burns for additional time to result in $\Delta$v savings. Further, this study showed that to achieve a smaller position dispersion (metric for uncertainty) at the end of the rendezvous profile, a higher number of observation burns resulted in smaller total $\Delta$v usage for dispersions less than approximately 1 km. It also indicated the upper and lower bounds for feasible values of time duration and position dispersions around which the total $\Delta$v grew rapidly. Finally, this study indicated that reducing the initial navigation error and initial state dispersions generally resulted in significant reductions in total $\Delta$v use. While the specific sensitivities in this notional angles-only scenario with its associated constraints may be unique to this case, the systematic process of evaluating an assortment of trajectory variations using a LinCov analysis in the loop with an optimization algorithm could be applied to develop robust, optimal rendezvous trajectories and to find desirable engineering trades for future missions to cislunar space.

## REFERENCES


[1] R. Whitley and R. Martinez, "Options for Staging Orbits in Cis-Lunar Space," *IEEE Annual Aerospace Conference*, Big Sky, MT, 2015.

[2] C. Jewison, *Guidance and Control for Multi-stage Rendezvous and Docking Operations in the Presence of Uncertainty*. PhD thesis, MIT, 2017.

[3] K. Mand, D. Woffinden, P. Spanos, and R. Zanetti, "Rendezvous and Proximity Operations at the Earth-Moon L2 Lagrange Point: Navigation Analysis for Preliminary Trajectory Design," *2014 AAS/AIAA Space Flight Mechanics Meeting*, Santa Fe, NM, AAS 14-376, 2014.

[4] D. Geller, S. Shuster, D. Woffinden, and S. Bieniawski, "Robust Cislunar Trajectory Optimization via Midcourse Correction and Optical Navigation Scheduling," *44th Annual AAS Guidance, Navigaiton and Control Conference*, Breckenridge, CO, AAS 22-065, 2022.

[5] D. K. Geller, "Linear Covariance Techniques for Orbital Rendezvous Analysis and Autonomous Onboard Mission Planning," *Journal of Guidance, Control, and Dynamics*, Vol. 29, November-December 2006, pp. 1404–1414.

[6] T. Goulet, D. Woffinden, N. Collins, and B. Andrews, "Robust Trajectory Design for Rendezvous in a Near-Rectlinear Halo Orbit," *AAS GN&C Conference*, Breckenridge, CO, AAS 23-066, 2023.

[7] G. Calkins, D. Woffinden, and Z. Putnam, "RRobust Trajectory Optimization for Guided Powered Descent and Landing," *2022 AAS/AIAA Astrodynamics Specialist Conference*, Breckenridge, CO, AAS 22-660, 2022.

[8] J. Joshi, D. Woffinden, and Z. Putnam, "End-to-End Mars Aerocapture Analysis Using Linear Covariance Techniques and Robust Trajectory Optimization," *2022 AAS/AIAA Astrodynamics Specialist Conference*, Charlotte, NC, AAS 22-678, 2022.

[9] J. W. Williams, W. E. Brandenburg, D. C. Woffinden, and Z. R. Putnam, "Validation of Linear Covariance Techniques for Mars Entry, Descent, and Landing Guidance and Navigation Performance Analysis," *AIAA Scitech 2022 Forum*, 2022.

[10] R. Chari, "Autonomous orbital rendezvous using angles-only navigation," 2001.

[11] D. Woffinden and D. Geller, "Observability Criteria for Angles-Only Navigation," *IEEE Transactions on Aerospace and Electrical Systems*, Vol. 45, July 2009, pp. 1194–1208.

[12] P. S. Maybeck, *Stochastic models, estimation, and control*, Vol. 1. New York: Academic Press, 1979.

[13] T. J. Moesser and D. K. Geller, "Guidance and Navigation Linear Covariance Analysis for Lunar Powered Descent," *AAS/AIAA Astrodynamics Specialist Conference*, Mackinac Island, Michigan, AAS 07-313, 19-23 August 2007.

[14] D. Geller and D. Christensen, "Linear Covariance Analysis for Powered Lunar Descent and Landing," *The Journal of Spacecraft and Rockets*, Vol. 46, Nov-Dec 2009, pp. 1231–1248.

[15] D. Woffinden, S. Robinson, J. Williams, and Z. Putnam, "Linear Covariance Analysis Techniques to Generate Navigation and Sensor Requirements for the Safe and Precise Landing - Integrated Capabilities Evolution (SPLICE) Project," *AIAA Scitech 2019 Forum*, San Diego, CA, AIAA 2019-0662, 7-11 January 2019 2019.

[16] N. Nise, *Control Systems Engineering*. Wiley, 2019.